Solid State Ionics 419 (2025) 116745

Contents lists available at ScienceDirect

Solid State Ionics

journal homepage: www.elsevier.com/locate/ssi

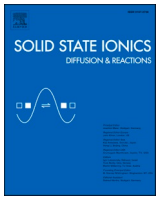

Tunable grain boundary conductivity in sodium doped high entropy oxides

Justin Cortez [a], Alexander Dupuy [a,b], Hasti Vahidi [a], Yiheng Xiao [a], William J. Bowman [a], Julie M. Schoenung [a,c,*]

[a] Department of Materials Science and Engineering, University of California, Irvine, Irvine, CA 92697, USA
[b] Department of Materials Science and Engineering, University of Connecticut, Storrs, CT 06268, USA
[c] Department of Materials Science & Engineering, and J. Mike Walker '66 Department of Mechanical Engineering, Texas A&M University, College Station, TX 77840, USA

ARTICLE INFO

Keywords:
High entropy oxides
Grain boundaries
Conductivity activation energy
Sodium-ion
Conductivity
Composition

ABSTRACT

Concerns with the safety and sourcing of lithium-ion batteries have prompted significant research into sodium-based systems. High entropy oxides (HEO), which contain five or more oxide components in equimolar amounts, are well suited for battery applications due to their ability to accommodate a substantial quantity of mobile charge carriers (such as sodium), while also demonstrating promising cycling stability, electrical conductivity, and battery capacity retention. Here we investigate the underexplored influence of sodium doping, processing, and microstructure on charge transport in bulk sintered $(Co,Cu,Mg,Ni,Zn)_{1-x}Na_xO$. We find that the conductivity increases with increasing dopant amount, up to 1.4×10^{-5} S•cm^{-1} at $x = 0.33$. Much of this increase is attributed to the high grain boundary conductivity, which originates from a Na_xCoO_2 layered structure that forms in the grain boundaries during processing. X-ray diffraction and transmission electron microscopy confirm the presence of the layered structure, while electrochemical impedance spectroscopy highlights the distinct contribution to the impedance response. The relative contributions of the grain boundaries and the bulk to the charge transport are discussed, along with how processing conditions and composition can be used to effectively engineer grain boundaries in doped HEO materials.

1. Introduction

The transition to renewable energy from fossil fuels requires inexpensive energy storage that is also safe and efficient. Significant research effort has been directed toward lithium-ion technology, which was first commercialized by Sony Co. in 1991 [1]. Modern lithium-ion batteries exhibit long service life, high power density, and excellent energy density [2,3]. However, lithium-ion batteries have significant issues, such as electrolyte flammability, toxicity, price, and possible challenges sourcing lithium [2,4]. Sodium-ion (Na-ion) batteries are a promising alternative due to their low price point, Na abundance, and faster electrode kinetics compared to lithium-ion batteries [5,6]. Additionally, all-solid-state Na-ion batteries have shown excellent durability, safety, and energy density [7,8]. However, there are still issues that hinder the cycling stability of all-solid-state Na-ion batteries, such as high reactivity of Na metal and battery capacity decline [6,9].

New strategies are needed to improve the cycling stability and capacity retention of solid-state Na-ion batteries. One promising design method is entropic stabilization. High entropy oxides (HEO) are composed of five or more oxide components in equiatomic concentrations, which form a single-phase solid-solution crystal structure after processing. One such HEO system is (Co,Cu,Mg,Ni,Zn)O (hereafter referred to as TM-HEO), which has demonstrated excellent cycling stability in lithium-ion battery applications [10–12]. In addition to cycling stability, high ionic conductivity is required of battery components to efficiently transport charge. Previous studies have shown that TM-HEO can accommodate a significant concentration of substitutional Na^+ cations while still maintaining its rocksalt crystal structure [13,14]. Several studies have also highlighted the promising ionic transport properties in TM-HEO systems when heavily doped with aliovalent alkali metals such as Li^+ and Na^+ [14–16]. Bérardan et al. found that bulk doped TM-HEO exhibited room temperature ionic conductivities greater than state-of-the-art lithium phosphorous oxy-nitride solid electrolytes [14]. For both aliovalent Na^+ and Li^+ dopants, their investigation revealed that ionic conductivity increases with increasing dopant amount. The authors attribute this increase in conductivity to the alkali

* Corresponding author at: 575 Ross St., College Station, TX 77843, USA.
E-mail address: schoenung@tamu.edu (J.M. Schoenung).

https://doi.org/10.1016/j.ssi.2024.116745
Received 20 May 2024; Received in revised form 25 November 2024; Accepted 26 November 2024
Available online 9 December 2024

metal occupying the lattice as substitutional cations. The aliovalent ions are hypothesized to travel through percolating paths assisted by the charge compensation mechanism and oxygen vacancies for ion transport [17].

While there has been important research on the effects of doping in TM-HEO on conductivity, as mentioned above, little work has been done to analyze this in conjunction with microstructure and processing. Bulk processing methods can produce varying microstructural features which play a critical role in the electrical behavior. For example, it is not unusual to encounter polycrystalline ionic materials with highly resistive grain boundaries that inhibit the overall conductivity of the bulk ceramic [18–21]. The electroceramic lithium lanthanum titanate is a prime example of a solid-state electrolyte that experiences a grain boundary blocking effect, which manifests as a grain boundary conductivity four orders of magnitude lower than that observed in the grain bulk [18]. The authors attribute this behavior to a positively charged boundary core that causes a depletion of lithium at the space charge layer. Vahidi et al. report that undoped bulk TM-HEO exhibits a decrease in grain boundary electronic conductivity along with a four order of magnitude increase in the grain bulk electronic conductivity, with the introduction of copper-rich secondary phases after post-sintering heat treatments [22]. The enhanced grain conductivity is attributed to the changes in grain defect chemistry, leading to an increase in electronic charge carrier concentrations (small polaron pairs). Similar effects may be present in other bulk polycrystalline alkali-based systems such as doped TM-HEO materials. Therefore, the possibilities for microstructure influence on doped polycrystalline TM-HEO are important to document for proper interpretation of measured results.

The rising need for lithium replacement and the promising electrical properties of TM-HEOs have led us to focus on this specific composition: $(Co,Cu,Mg,Ni,Zn)_{1-x}Na_xO$ (hereafter referred to as Na-HEO). The proven high ionic conductivities and potential cycling stability of bulk TM-HEO have garnered significant interest, yet the understanding of how doping, composition, and microstructure affect the electrical behavior is incomplete. In this work, we study bulk Na-HEO by altering dopant concentration, x, and varying the grain size across three regimes: fine grain, intermediate grain, and coarse grain. We find that dopant amount and processing conditions significantly influence the microstructure evolution, electrical behavior, and charge transport mechanisms. We then compare the results of our Na-HEO materials with other bulk polycrystalline ionically conductive ceramics.

2. Experimental methods

Bulk Na-HEO samples were prepared using solid-state powder synthesis. The constituent oxide powders were purchased from US Research Nanomaterials (Houston, TX, USA) as CoO (50 nm particle size, 99.7 wt %), CuO (22–55 nm, 99.95 %), MgO (50 nm, 99.95 %), NiO (18 nm, 99.98 %), and ZnO (18 nm, 99.95 %), while the carbonate powder was purchased from Sigma-Aldrich (St. Louis, MO, USA) as Na_2CO_3 (99.999 %). Four separate powder compositions were prepared to create Na concentrations of 0 mol% (undoped), 8 mol%, 16 mol% (equimolar), and 33 mol%. The specific HEO compositions were chosen to obtain a representative upper and lower value relative to the equimolar composition. Each powder composition was separately blended using planetary ball milling (PBM) in a Premium 7 (Fritsch GmbH, Idaroberstein, Germany) at 300 rpm for 3 h using silicon nitride jars and milling media. The as-milled powders were heat treated at 950 °C for 50 min to create single-phase Na-HEO rocksalt powders. These pre-reacted powders were again separately milled at 300 rpm for 12 h for further particle size reduction.

Each composition of Na-HEO was processed to achieve bulk samples with one of three grain size regimes: fine grain (FG), intermediate grain (IG), and coarse grain (CG). The pre-reacted Na-HEO powders were densified into fine and intermediate grain size samples using a Fuji model 825S (Fuji, Saitama, Japan) spark plasma sintering (SPS) instrument. The samples were heated to a maximum sintering temperature of 700 °C at a heating rate of 200 °C/min under a pressure of 100 MPa. The powders were held at this temperature for 5 min and then cooled down at a rate of 50 °C/min. Samples polished after this step were used as fine grain samples. Intermediate grain size samples were heat treated after SPS using a CM Furnaces 1210BL elevator furnace (Bloomfield, NJ, USA) at 900 °C for 1 h in air, and then subsequently polished. Coarse grain size samples were prepared by first consolidating by SPS at 600 °C for 5 min and 100 MPa. These samples were then conventionally sintered in the elevator furnace at 1000 °C for 1 h. All samples are summarized in Table 1 and follow the labeling scheme: Grain size (FG, IG, CG) – Na mol% (0, 8, 16, 33) – HEO.

The phase state of the powder and bulk samples was determined by using X-ray diffraction (XRD) conducted using a Rigaku Ultima III diffractometer (Rigaku, Tokyo, Japan). Rietveld refinement of the XRD patterns was used to determine the lattice parameter of each sample using the program *MAUD* (Materials Analysis Using Diffraction) [23], and then subsequently the theoretical density. Geometric density measurements were used to acquire the relative density of the bulk samples, assuming theoretical density values of 6.137, 6.065, 6.001, and 5.886 g/cm^3 as calculated for the four compositions studied: 0, 8, 16, and 33 mol % Na, respectively. Microstructure analysis of the samples was performed using a Tescan GAIA3 GMH FIB-SEM (Brno, Czech Republic) scanning electron microscope (SEM). The average grain size of the sintered specimens was determined through SEM analysis of fracture surfaces. Scanning transmission electron microscopy (STEM) imaging in high-angle annular dark-field (HAADF) and bright-field (BF) coupled with energy-dispersive X-ray spectroscopy (STEM-EDS) using a JEOL Grand ARM (Akishima, Tokyo, Japan) at 300 kV was performed to examine the structure and composition of the grain boundaries in the bulk samples. The following peaks were used for the analysis: O *Kα* (0.525 keV), Mg *Kα* (1.254 keV), Ni *Kα* (7.480 keV), Co *Kα* (6.931 keV), and Kβ (7.649 keV), Cu *Kα* (8.046 keV) and Kβ (8.904 keV), and Zn *Kα* (8.64 keV) and Kβ (9.570 keV). TEM samples were prepared using the focused ion beam (FIB) lift out technique.

X-ray photoelectron spectroscopy (XPS) was performed using a Kratos AXIS-Supra system (Trafford Park, Manchester, UK) fitted with a monochromatic Al Kα X-ray source at 225 W and a base pressure of 5E-9 Torr. The bulk sample surfaces were cleaned with 5 keV Ar^+ ion etching before XPS to remove any contamination. The survey scans used 160 eV pass energy and 1 eV energy step, while detailed scans used 20 eV pass energy with a 0.1 eV energy step. Photoelectrons were collected using a hemispherical analyzer in conjunction with a charge neutralizer.

Electrical properties of the undoped and doped samples were measured using a Bio-Logic SP-200 potentiostat. To record the electrical response, we used an oscillation voltage of 500 mV and a frequency range of 200 mHz – 3 MHz. A 500 mV AC amplitude was selected to be consistent with other work on the electrical behavior of TM-HEO [14,24]. Samples had wire contacts glued to each side with silver paste to form metal-insulator-metal cells. Total, grain boundary, and grain bulk conductivities were determined through equivalent circuit fitting of Nyquist plots from electrochemical impedance spectroscopy (EIS). It is important to note that grain boundary conductivities reported in this study were calculated based on the sample dimensions instead of the grain boundary geometry and are thus effective (or apparent) grain

Table 1
| Labels for each sample of varying grain size and dopant concentration.

$(Co,Cu,Mg,Ni,Zn)_{1-x}Na_xO$	x = 0.0	x = 0.08	x = 0.16	x = 0.33
Fine grain	FG-HEO	FG-8Na-HEO	FG-16Na-HEO	FG-33Na-HEO
Intermediate grain	IG-HEO	IG-8Na-HEO	IG-16Na-HEO	IG-33Na-HEO
Coarse grain	CG-HEO	CG-8Na-HEO	CG-16Na-HEO	CG-33Na-HEO

boundary conductivities. Traditional double Randles cell circuits were used for undoped and lightly doped samples, while samples with higher doping amounts and apparent diffusion effects used an additional constant phase element in series. The activation energy (E_a) of each sample was determined from the Arrhenius equation, with EIS measurements conducted at temperatures of 20 °C to 100 °C (with 20 °C steps).

3. Results

3.1. Microstructure, phase state, and oxidation states

The microstructure for each sample exhibits grains that are relatively equiaxed, such as those shown in the SEM micrographs for samples FG-16Na-HEO, IG-16Na-HEO, and CG-16Na-HEO are provided in Fig. 1 A-C, respectively. The average grain size values range from 0.10 to 0.25 μm (100 to 250 nm) for the fine grain (FG) samples, from 1.5 to 3.2 μm for the intermediate grain (IG) samples, and from 6.3 to 8.2 μm for the coarse grain (CG) samples, as summarized in Table 2.

All bulk samples exhibit relative density values greater than 75 %, as indicated in Table 2, which are comparable to values reported by Bérardan et al. [14]. The bulk samples also exhibit intense XRD peaks corresponding to the planes of the rocksalt crystal structure (Fig. 1D - G). Small secondary phase peaks can be observed in the FG samples, corresponding to the Cu-rich tenorite phase. Our previous work has shown that this Cu-rich tenorite secondary phase forms when TM-HEO is processed at temperatures less than 850 °C [25].

Rietveld refinement of the bulk Na-HEO XRD patterns allows for the calculation of the lattice parameter. Bulk Na-HEO samples exhibit a decreasing trend in lattice parameter with increasing dopant concentration (see Table 2), indicating that the Na is dissolving into the rocksalt solid-solution. This behavior is consistent with previous studies on Na-doped TM-HEOs [13,14], where it is demonstrated that the contraction in lattice parameter could be due to multiple factors, such as changes in oxidation states or the formation of oxygen vacancies. The possible changes in oxidation state of cation species is significant, as these changes can influence the electoral behavior in oxide materials [26,27].

XPS was used to acquire information on the cation valence state in the Na-HEO samples and provides insight into the decrease in lattice parameter in doped samples. High resolution scans seen in Fig. 2 are for the Co-2p core level spectra of IG-HEO, IG-8Na-HEO, IG-16Na-HEO, and IG-33Na-HEO, which exhibit dominantly the Co^{2+} state. The main peak

Table 2
| Average grain size, relative density, and lattice parameter for bulk TM-HEO and Na-HEO samples.

	Average Grain Size (μm)	Relative Density	Lattice Parameter (nm)
FG-HEO	0.11 ± 0.05	0.954	0.4237
IG-HEO	1.54 ± 0.73	0.978	0.4238
CG-HEO	9.43 ± 4.31	0.997	0.4238
FG-8Na-HEO	0.25 ± 0.05	0.889	0.4237
IG-8Na-HEO	2.89 ± 1.13	0.874	0.4237
CG-8Na-HEO	6.34 ± 1.97	0.946	0.4236
FG-16Na-HEO	0.21 ± 0.07	0.863	0.4236
IG-16Na-HEO	3.16 ± 1.21	0.814	0.4236
CG-16Na-HEO	7.81 ± 1.01	0.937	0.4234
FG-33Na-HEO	0.25 ± 0.09	0.754	0.4237
IG-33Na-HEO	2.35 ± 0.94	0.796	0.4236
CG-33Na-HEO	8.20 ± 2.13	0.998	0.4236

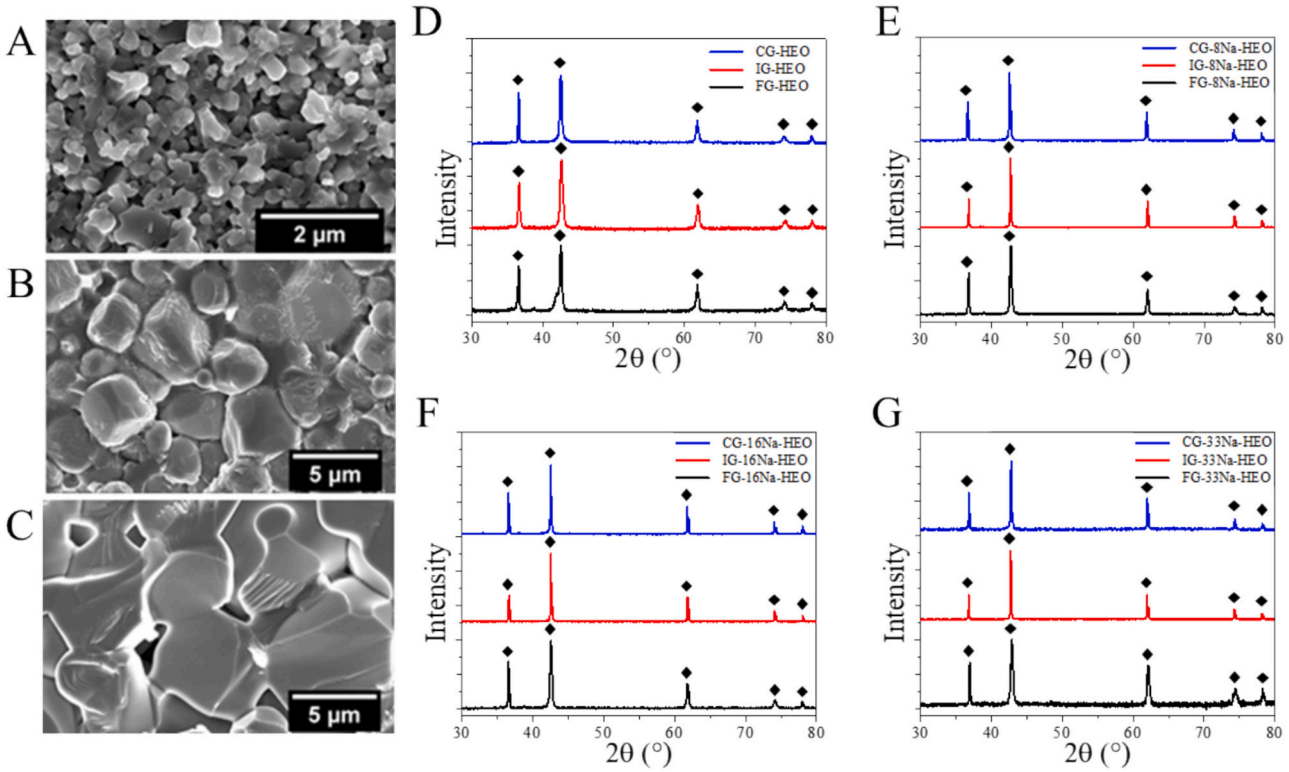

Fig. 1. (A-C) Micrographs of equimolar 16Na-HEO for: (A) FG-16Na-HEO, (B) IG-16Na-HEO, and (C) CG-16Na-HEO samples. (D-G) XRD patterns for: (D) undoped Na-HEO, (E) 8Na-HEO, (F) 16Na-HEO, and (G) 33Na-HEO. Each chart contains patterns for fine grain, FG (black), intermediate grain, IG (red), and coarse grain CG (blue) samples. The diamonds identify the rocksalt peaks.

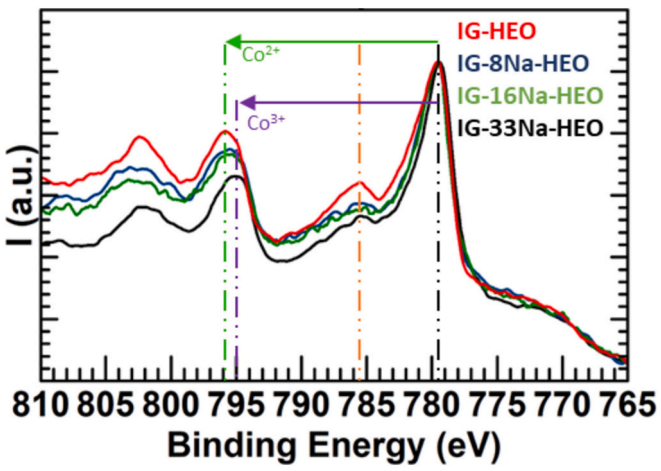

Fig. 2. Co-2p core level spectra for IG-HEO (red), IG-8Na-HEO (blue), IG-16Na-HEO (green), and IG-33Na-HEO (black) with corresponding Co^{2+} (green) and Co^{3+} (purple) peak distances.

is at approximately 780 eV, and satellite peaks are visible at ~786, ~796, and ~803 eV. The binding energy difference between the main peak at 780 eV and its satellite near 796 eV can indicate the presence of Co^{3+}, with smaller binding energy differences indicating a greater likelihood of the Co^{3+} state [28]. The binding energy difference decreases from 15.8 eV (indicating Co^{2+}) in IG-HEO to 15.0 eV in the IG-33Na-HEO sample, suggesting the presence of Co^{3+} [28]. Further evidence of cobalt oxidation is indicated by the increase in the difference in binding energy between the satellite peaks at 795 eV and 803 eV [29]. The satellite peak shown in Fig. 2 at 786 eV highlighted by an orange line also signifies the presence of Co^{2+} [29]. The addition of 8 mol% Na immediately begins to depress this satellite peak at 786 eV and signifies the partial oxidation of $Co^{2+}$to Co^{3+}. Other cations of interest, such as Ni^{2+}, demonstrate minimal-to-no change in oxidation state with the introduction of Na into the material (Fig. S1 in the Supplementary Material).

3.2. Grain boundary structure

High-angle annular dark field (HAADF) and bright field (BF) STEM micrographs for sample IG-16Na-HEO (Fig. 3 A & B) show the grain boundary structures at higher magnifications. A thick (~5 nm) secondary phase with a layered structure is observed in the grain boundaries while the grain bulk maintains the rocksalt crystal structure (Fig. 3C & D). To our knowledge, such a structure has not been observed in the TM-HEO material before. STEM-EDS performed at the boundary (Fig. 3 E & F) shows that the layered structure is mainly occupied by Co and Na layers (STEM-EDS spectrum is provided in Fig. S2). The Na appears to be in a separate layer from the Co, while the other transition

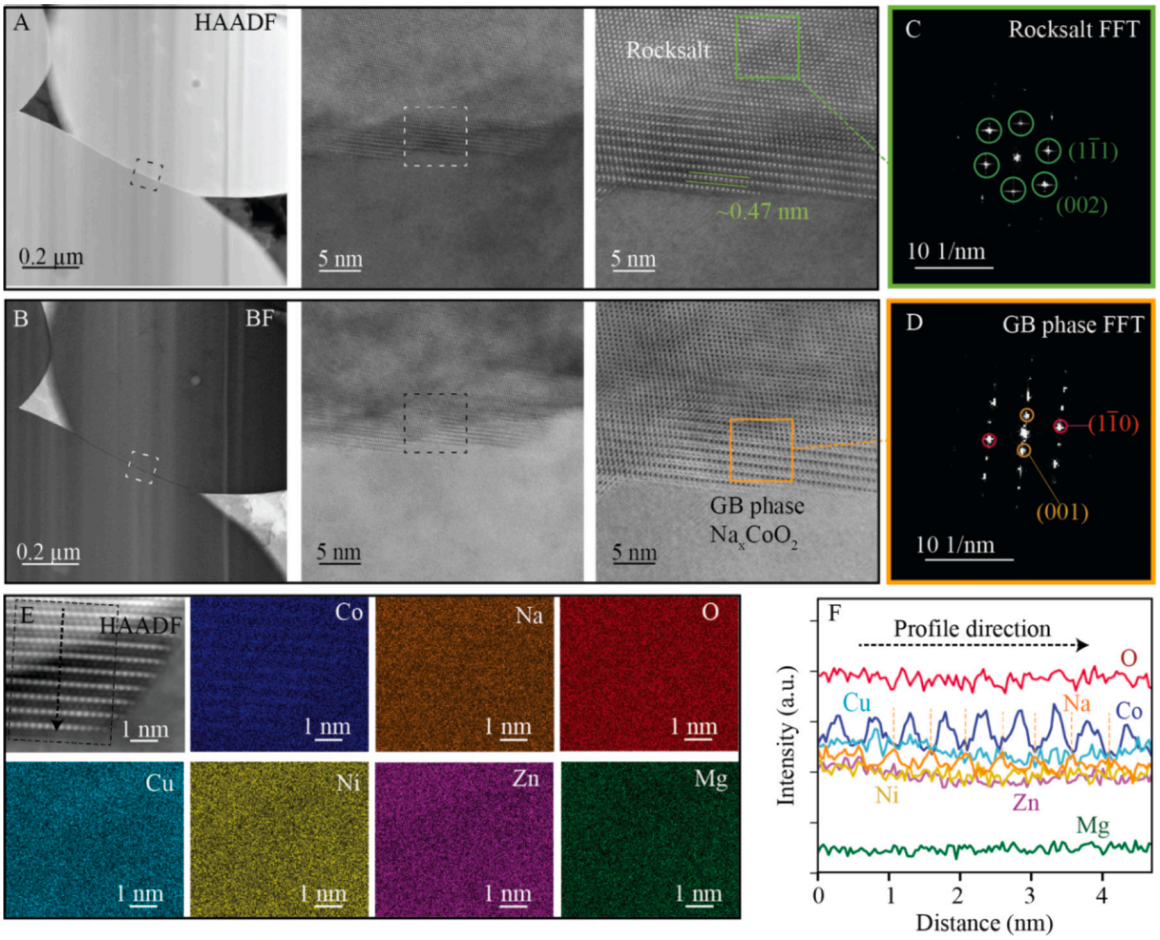

Fig. 3. (A) HAADF-STEM and (B) BF-STEM micrographs of equimolar Na-HEO grains and grain boundaries enriched with the layered grain boundary phase. Higher magnification micrographs of the region highlighted by the dotted squares are provided. Fast Fourier transform patterns of (C) the rocksalt matrix and (D) the grain boundary phase structure is determined using an isolated part of the atomic-resolution images highlighted with green and orange squares, respectively. (E) STEM-EDS chemical maps of the grain boundary phase using O K, Na K, Mg K, Co K, Ni K, Cu K and Zn K characteristic X-ray energies. (F) STEM EDS line scan results from (E) showing intensities of oxygen and cations. The black dotted arrow and square denote the region where the STEM EDS line scan was performed.

metals have much lower intensities.

Fast Fourier transform patterns calculated using a portion of the atomic-resolution STEM HAADF images yield the patterns shown in Fig. 3D, which suggest that the grain boundary layer phase has a P2 type structure. The presence of the alternating Na and Co layers, along with the P2 Fourier transform pattern indicate that the layered structure in the grain boundary is a form of Na_xCoO_2. The Na_xCoO_2 compound is a well-studied layered structure known for its ability to transport Na^+ [30], as well as possible superconducting properties [31], and has been used as a cathode material in Na-ion batteries [32]. We hypothesize that the P2 structure forms at most grain boundaries in our Na-doped TM-HEO samples. In our previous work, we observed that undoped TM-HEO forms a Cu-rich tenorite phase during heat treatment [25]. This tenorite secondary phase forms extensively in the grain boundaries of TM-HEO [33]. The grain boundaries of TM-HEO serve as high energy defects which are amenable to the segregation of cations and the nucleation of secondary phases.

Na_xCoO_2 can form four distinct crystal structures: P2, P′3, O3, and O′3 [34]. However, a pure P2 structure typically forms at higher temperatures (> 750 °C) and is considered to be more stable during intercalation than the other polymorphs [34,35]. The FG samples in the current study show no major P2 Na_xCoO_2 XRD peaks, likely due to the lower processing temperatures and short processing times. We hypothesize that the transformation kinetics are too slow at 700 °C to meaningfully form the Na_xCoO_2 phase in the FG samples. The IG samples do not show the P2 phase XRD peak either, but TEM confirms its presence at grain boundaries (Fig. 3). Finally, the CG samples have a high enough concentration of Na_xCoO_2 to be detected by XRD, as seen in the XRD pattern for CG-16Na-HEO (Fig. S3). Rietveld refinement of the sample indicates that there is ~1 at.% of the P2 $NaCoO_2$ in sample CG-16Na-HEO. We also note that some Cu is detected in this layered structure at the grain boundary (Fig. 3F). We attribute the presence of Cu to the solubility of Cu in $NaCoO_2$. Although the exact solubility of Cu in $NaCoO_2$ is not known, many authors have explored Cu-doped $NaCoO_2$. Several studies have found that $NaCo_{1-x}Cu_xO_2$ can accommodate values of x = 0.3 [36,37].

3.3. Electrical properties

Electrical measurements on the twelve TM-HEO samples indicate a range of electrical behavior. The general trend for Nyquist plots among the various samples is a singular arc response for undoped samples to multi-arc behavior for doped samples and even some undoped coarse grain samples. For brevity, two representative data sets for FG-Na-HEO samples are displayed as Nyquist plots in Fig. 4 (data for all 12 samples are provided in the Supplementary Material Fig. S5). Undoped FG-HEO (Fig. 4 A) exhibits a singular arc, while doped FG-8Na-HEO (Fig. 4B, inset in Fig. 4 A) differs in that two arcs are present and at much lower values of impedance. The difference in impedance between undoped and doped is so large, that the doped plot is not visible. Fig. 4B shows the magnified section of the FG-8Na-HEO Nyquist plot in red. The appearance of an additional arc in the doped sample indicates multiple conduction processes, such as charge transport through the grain bulk and grain boundary [38,39].

To determine the role of microstructure on electrical conductivity, each Nyquist plot was fit with an equivalent circuit to isolate the charge transport response within the sample. The equivalent circuit used is shown in inset (B) of Fig. 4. The rectangular R components represent a resistor and the arrowed Q components represent a constant phase element, which accounts for the non-ideality of a capacitor [14,40]. The circuit has demonstrated to effectively fit the impedance response and characteristic semicircles that are often observed in the Nyquist plots of metal oxides [39]. Of relevance to this study, this circuit can be used to differentiate the contributions of the grain boundary and the grain bulk to the electrical behavior in oxide materials [39,40]. The resistor R1 is associated with a frequency independent resistance commonly referred

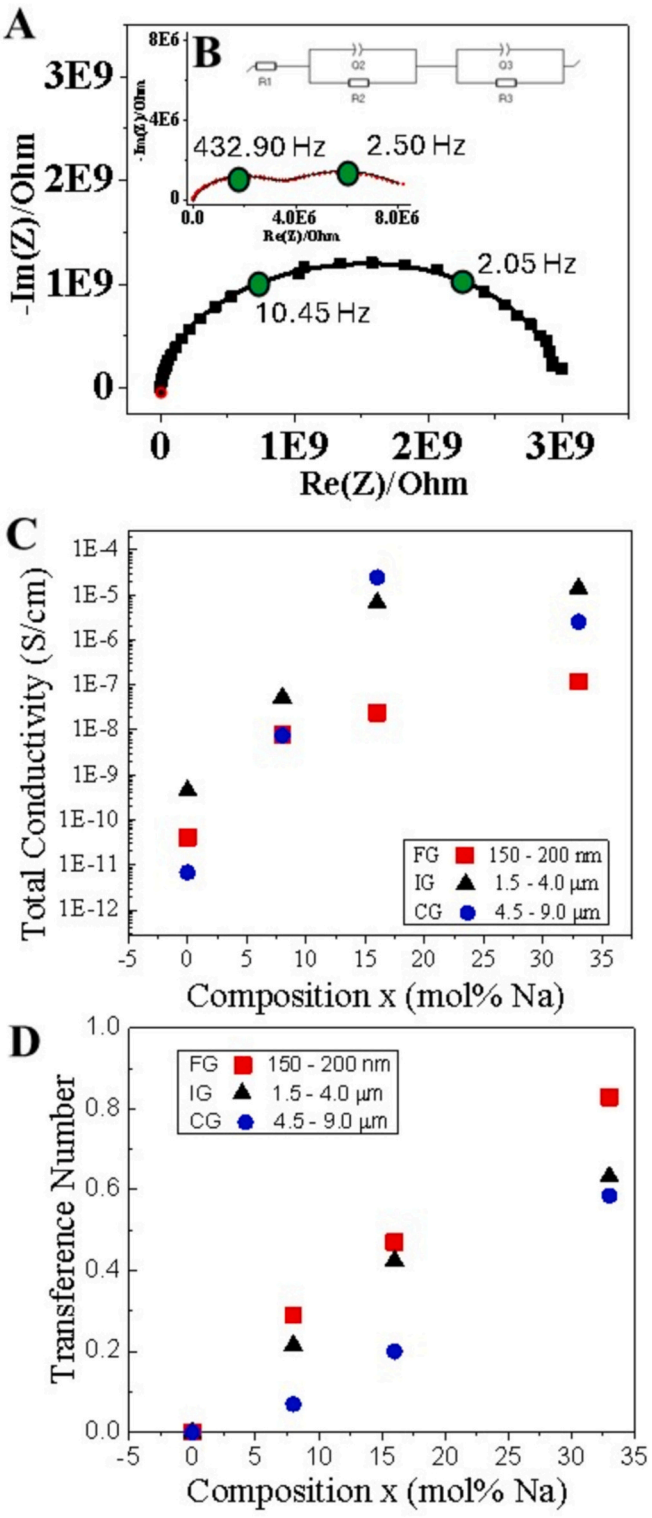

Fig. 4. (A) Nyquist plots for FG-HEO and FG-8Na-HEO bulk samples. Experimental data are represented by black squares and red circles for samples FG-HEO and FG-8Na-HEO, respectively, and the equivalent circuit fit data are shown as black lines. Inset (B) is the magnified view for FG-8Na-HEO, with the equivalent circuit used for fitting. The green circles denote the characteristic frequencies associated with the Randles cell semicircles. The characteristic frequency values are labeled adjacent to the circles. (C) Total conductivity values for fine grain (FG) in red, intermediate grain (IG) in black, and coarse grain (CG) samples in blue, as a function of Na content. (D) Transference number.

to as the solution resistance. The solution resistance or electrolyte resistance is the high frequency impedance associated with the electrolyte resistance between the working and reference electrodes [41]. The parallel R2 and Q2 (Randall cell) represent the high frequency resistance and capacitance response related to the grain bulk. The R3 and Q3 components account for the grain boundary response [39]. The double Randall cell equivalent circuit, which has been used for Na-doped TM-HEOs in the past [14], was therefore used to compute the total, grain bulk, and effective grain boundary conductivity [20]. Equivalent circuit fits for the two representative samples can be seen in Fig. 4 A & B as a black line. The selected equivalent circuit model fits the data well and shows little deviation.

Total conductivity values measured from the equivalent circuit analysis show an increase in conductivity with increasing Na content (Fig. 4C). When compared to the doped samples in this study, undoped TM-HEOs exhibit the lowest total conductivity ranging from 6.8×10^{-12} to 4.1×10^{-11} S•cm^{-1} depending on the grain size. The conductivity significantly increases with the introduction of Na into the material. The conductivity of the FG samples increases after doping (up to 1.2×10^{-7} S•cm^{-1}). The IG samples also demonstrate a significant increase in conductivity with increasing Na content (up to 1.4×10^{-5} S•cm^{-1}), but analogous to the CG samples (which exhibit a maximum conductivity of 2.4×10^{-5} S•cm^{-1}), these samples exhibit a plateau in conductivity at and above 16 mol% dopant concentration. Similar results have been seen in Li- doped TM-HEOs, where above 20 mol% doping, the conductivity increase begins to plateau [15,16]. The ionic transference number of our Na-doped TM-HEO samples was calculated using the method outlined in Moździerz et al. on Li-doped TM-HEO [24]. The transference number data can be seen in Fig. 4D. We first note that all of the samples in this study have a transference number < 1, indicating they are mixed ionic-electronic conductors. Increased Na concentration leads to an increase in the transference number, which is in agreement with previous work on the Li-doped TM-HEO [24]. We also observe that samples with finer grain sizes have greater transference numbers compared to samples with more coarse grain sizes. An increase in the ionic transference number with increasing grain size has been observed before in other ionic conducting ceramics [42,43].

Equivalent circuit analysis showed that grain bulk conductivity (σ_b) and effective grain boundary conductivity (σ_{gb}) for all samples demonstrated a generally increasing trend with doping (Fig. 5). For FG Na-HEO, the value for σ_{gb} is shown to be lower than the value for σ_b for all dopant concentrations (Fig. 5 A). However, there is still a significant increase in both σ_b and σ_{gb} with increased dopant concentrations. The IG and CG samples show a different trend, where the value for σ_{gb} at higher dopant concentrations is greater than the value for the bulk (Fig. 5 B & C).

As mentioned in Section 2, our reported grain boundary conductivity values are calculated based on the dimensions of the bulk sample and thus represent an effective grain boundary conductivity. We calculated the true grain boundary conductivity using a standard brick and mortar model [44]:

$$\sigma_{gb,t} = \frac{\delta}{D}\sigma_{gb,a} \tag{1}$$

where $\sigma_{gb,t}$ is the true grain boundary conductivity, δ is the grain boundary thickness, D is the average grain size, and $\sigma_{gb,a}$ is the apparent grain boundary conductivity. Previous work has found that the undoped TM-HEO has a value of $\delta \approx 1$ nm [22]. Our TEM results from the current study indicate that $\delta \approx 5$ nm for Na-doped TM-HEO samples. Our calculated $\sigma_{gb,t}$ values are several orders of magnitude smaller than the measured $\sigma_{gb,a}$ and σ_b values for all of our samples (Table S1). The low $\sigma_{gb,t}$ values are unsurprising given how thin the grain boundary and boundary layer phases are in comparison to the grain size. Notably, the values for $\sigma_{gb,t}$ do not modify any of the observed trends. Thus, we continue to use the effective grain boundary conductivity for the remainder of the discussion.

Porosity can influence the electrical behavior of ceramics. A calculation was performed to account for the role of porosity on conductivity using the Bruggeman effective medium theory [45]. The Bruggeman theory has been previously applied to TM-HEO [24], and uses the following equation:

$$\sigma_m = \sigma_h\left(1 - \frac{3}{2}f\right) \tag{2}$$

where σ_m is the measured total conductivity, σ_h is the porosity corrected conductivity, and f is the porosity. We observe that the measured and corrected conductivity values are similar (Table S2), with the conductivity values changing by less than an order of magnitude after correction. Most importantly, we observe that the porosity correction does not influence the overall trends in our data. We conclude that the presence of porosity in our samples does not meaningfully influence the interpretation of our results. As a result, we have left the uncorrected values in the main body of the manuscript.

4. Discussion

4.1. Na-HEO charge compensation

We hypothesize that doping TM-HEO (cation valence +2) with Na (cation valence +1) will stimulate two possible charge compensation mechanisms: formation of oxygen vacancies and oxidation of a transition metal cation, as noted below in eqs. (3) and (4) respectively:

$$Na_2O \Rightarrow_{TM-HEO} 2Na'_M + V_O^{\bullet\bullet} + \frac{1}{2}O_{2(g)} \tag{3}$$

$$Na_2O \Rightarrow_{TM-HEO} 2Na'_M + 2M_M^{\bullet} + \frac{1}{2}O_{2(g)} \tag{4}$$

Table 2 shows that the lattice parameter of Na-HEO decreases slightly with the addition of Na, which is consistent with previous

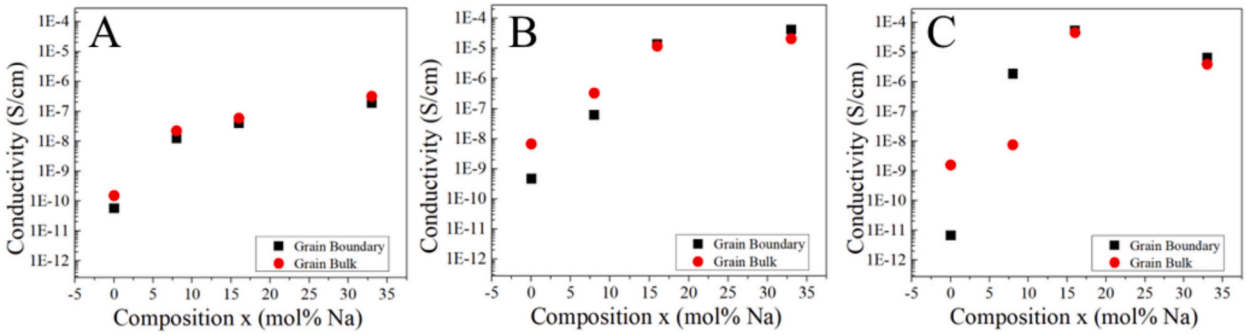

Fig. 5. Conductivity values for: (A) fine grain size (FG), (B) intermediate grain size (IG), and (C) coarse grain size (CG) samples. The effective grain boundary values are represented as black squares; the grain bulk values are represented as red circles.

reports on lithium-doped TM-HEOs [13,15,16]. The decrease in lattice parameter is initially unexpected due to Vegard's Law [46], as the ionic radius of Na^+ is larger than that of the other transition metal cations. According to Vegard's Law, the expected lattice parameter values for 0, 8, 16, and 33 mol% Na should be 0.425, 0.430, 0.434, and 0.444 nm, respectively. Previous studies reported that for TM-HEOs doped with aliovalent Li^+ or Na^+, the Co^{2+} ion consistently transforms into the Co^{3+} state to maintain charge neutrality [15,16]. While not as prevalent as Co oxidation, there is also evidence of Ni^{2+} transformation to the Ni^{3+} state in Na-doped TM-HEO [13]. Nickel 2p core spectra typically exhibit a broadening of the main peak for Ni^{3+}, which is not present in our data (Fig. S1C in Supplementary Material) [47]. Copper 2p core level spectra from the current study indicate signs of a mixed Cu^{1+} and Cu^{2+} oxidation state (Fig. S1B in Supplementary Material), which has been observed before in TM-HEO [16,22,48]. Notably, the measured spectra do not show any significant variation with Na addition. Overall, the oxidation of Co (Fig. 2) seems to be the dominant charge compensation mechanism for strain relief and charge neutrality, which may assist in the percolation of Na^+ or electron transport [15].

The role of dopant on electrical behavior in TM-HEO is not fully understood. Previous work attributed the increase in total conductivity of aliovalent-doped TM-HEOs to the increase in mobile charge carrier ions percolating through oxygen vacancies created by a charge compensation mechanism [14]. However, Osenciat et al. showed that there is no increase in oxygen vacancy formation with the addition of an aliovalent ion (Li^+) until concentrations greater than 20 mol% are reached [16]. Above this doping concentration, the vacancy formation steadily increases, and there is a reduced dependence of conductivity on dopant concentration, which is consistent with our observations in highly Na-doped TM-HEO samples (e.g., samples IG-16Na-HEO and IG-33Na-HEO in Fig. 4C). A more recent study on Li-doped TM-HEO examined the role of pressure on ionic conductivity [49]. The authors observed that the ionic conductivity decreased with increasing pressure. Li-doped HEO was found to have an activation volume of 1.14 cm^3/mol, which is similar to fast ionic conductors which exhibit a lattice dilation effect during ionic conduction [50,51].

Strain measurements from Moździerz et al. demonstrate a rise in lattice strain in 20 mol% Li-doped TM-HEO, and significant strain relief after additional doping [15]. It was hypothesized that Li-doped TM-HEOs produce strain from a charge compensation mechanism. However, above the 20 mol% limit the lattice cannot distort further, so the aliovalent dopant is compensated with the formation of oxygen vacancies. The rise in lattice strain has also been observed in Na-doped TM-HEO, indicating the presence of a similar mechanism [13]. Additionally, previous studies on similar Na-doped and Li-doped TM-HEO compositions indicate negligible loss of Na or Li during sintering at 1000 °C for 12 h [14,52]. Our study involves processing at lower temperatures (700–1000 °C) for short periods of time ($\leq$ 1 h). We therefore conclude that our samples experience minimal Na loss during our processing steps.

4.2. Na-HEO conductivity

In general, our samples demonstrate an increase in conductivity with increases in dopant concentration (Fig. 4C). Notably, the larger grain size samples show orders of magnitudes greater conductivity for highly doped samples when compared to fine grain samples (Fig. 4C). The difference in conductivity is likely due to the high grain boundary conductivity for highly doped intermediate and coarse grain samples (Fig. 5B & C), indicating enhanced boundary charge transport.

We propose that the layered structure in the grain boundaries contributes to an increase in Na^+ transport in our Na-HEO samples, and ultimately enhances the total and effective grain boundary conductivity values. Lei et al. proposed that entropy stabilization can assist in the formation of a P2-type structure due to the higher processing temperatures, off stoichiometry, and greater entropy [34]. Comparable behavior is also seen to be possible in other medium [53] and high entropy [54,55] layered Na-based cathode materials, which show enhanced cycling stability and Na^+ transport. Therefore, we expect that the presence of the P2 layered structure at the boundary will significantly influence the grain boundary conductivity. The different values of σ_{gb} for samples FG-8Na-HEO and CG-8Na-HEO (Fig. 5 A & C) highlight three possible requirements for the occurrence of this layered structure. First, the sample must have sufficient Na for the layered structure to form at the boundary, second the processing temperature must be high enough to stimulate the formation of the layer-structured secondary phase, and third sufficient time at temperature must be provided. The effective grain boundary conductivity in sample FG-8Na-HEO is less than the bulk conductivity (Fig. 5 A), which we attribute to insufficient Na content, the lower processing temperature, or inadequate time at temperature. However, Lei et al. found that the P2 phase forms with considerable off-stoichiometry in the Na_xCoO_2 composition, specifically $0.68 < x < 0.76$ [34]. The lack of boundary phase in FG-8Na-HEO is, therefore, unlikely to be due to insufficient Na. In contrast, sample CG-8Na-HEO (Fig. 5C) demonstrates enhanced effective grain boundary conductivity at 8 mol% Na, indicating that this dopant level is sufficient for enhanced effective grain boundary conductivity in this sample. Thus, the formation of the boundary structure may stem from the higher processing temperatures or longer processing times used to make this sample. Pure P2 Na_xCoO_2 has a higher likelihood of forming above 750 °C, with lower temperatures resulting in a mixture of the P2, P3, and O3 type structures [34]. The fine grain samples, which are processed at 700 °C, may not reach the temperatures required to form the P2 phase. To determine if processing temperatures above 750 °C or longer heating times are required for the formation of the Na_xCoO_2 boundary phase in Na-HEO, we heat treated an equimolar fine grain Na-HEO sample at 700 °C for 12 h. Peaks associated with the Na_xCoO_2 phase, as well as additional secondary phase peaks, were observed in the XRD pattern after the 12 h heat treatment. Thus, kinetics play a role in the formation of this phase, and fine grain samples with the boundary structure may be prepared with appropriate processing conditions. The observed phase is in agreement with other studies that found it is possible to form P2 Na_xCoO_2 at or above 650 °C under specific conditions [34,56].

4.3. Bode plot analysis

Bode plots of the impedance data were analyzed to examine the frequency dependance of the electrical behavior. Representative Bode magnitude and Bode phase plots for samples FG-HEO, FG-33Na-HEO, CG-HEO, and CG-33Na-HEO can be seen in Fig. 6. Changes in the phase angle are indicative of changes to mechanisms contributing to the electric response, while the magnitude of the impedance can reveal information about the contributions to the electrical conductivity [57].

The Bode plots allow for interpretation of impedance contributions in the time domain, which can allow for identification of conductivity mechanisms based on their distinct time constants. Goswami et al. developed a theoretical approach for defining the different mechanisms occurring within the system by analyzing Bode plot impedance data [57,58], which we use here. For the purposes of simplifying the interpretation, we divide the Bode plots into three frequency regimes. These three frequency regimes are shown in Fig. 6: (1) the low frequency regime ($\sim <$ 1 log Hz) attributed to the interface between the electrode and sample (highlighted in blue), (2) an intermediate frequency regime ($\sim$ 1–5 log Hz) related to the transfer of ions across the grain and grain boundary (gray), (3) and a high frequency regime ($\sim >$ 5 log Hz) associated with the relaxation of ions in the grain and relaxation of the space charge layer in the grain boundaries (orange) [57–59]. A high magnitude of impedance for the FG undoped samples is observed at low frequencies (Fig. 6 A), which we attribute to the sluggish charge transfer at the electrode and electrolyte interfaces [57,58]. The relatively high impedance in the intermediate frequency regime is ascribed to the highly resistive grain boundaries, as grain boundaries in oxide materials

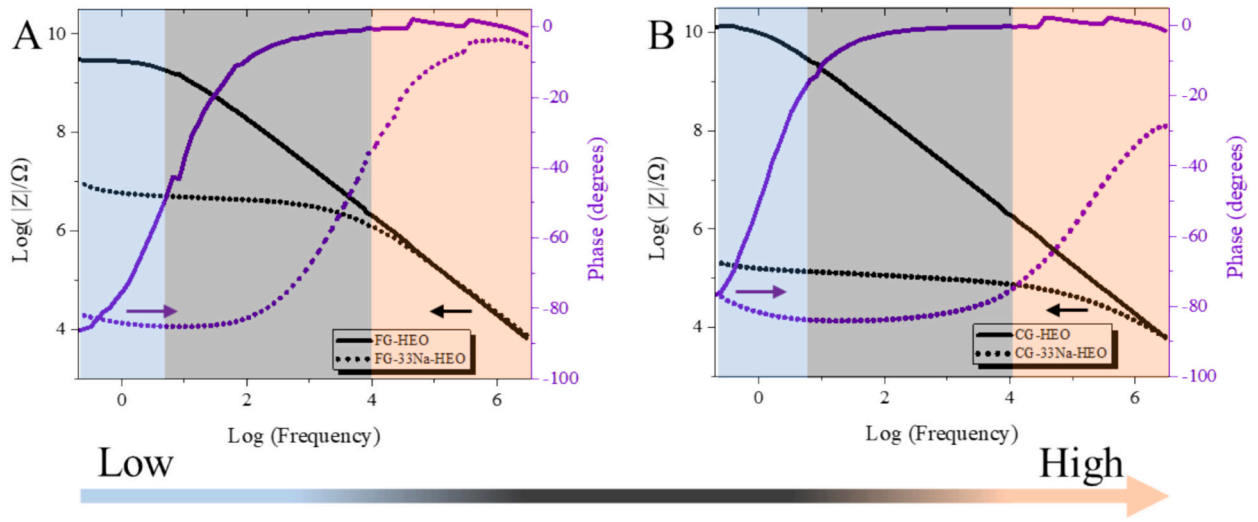

Fig. 6. Bode plots for (A) fine grain and (B) coarse grain samples. Magnitude of impedance is plotted in black, while phase angle is shown in purple. The solid lines represent undoped samples (FG-HEO and CG-HEO, respectively) and the dashed lines represent Na-doped samples (FG-33Na-HEO and CG-33Na-HEO, respectively). Lastly, the frequency is separated into three regimes: low (blue), intermediate (gray), and high frequency (orange).

typically behave as insulating layers [18,39,60]. Finally, we observe lower magnitudes of impedance in the high frequency regime related to the relaxation of ions in the grain. For the FG samples, the introduction of Na depresses the impedance magnitude in the low and intermediate frequency regimes compared to the undoped sample, alluding to a more ohmic metal electrolyte interface and grain boundaries. The change in impedance response with doping is more pronounced in the CG samples (Fig. 6B) compared to the FG samples. The intermediate frequency regime exhibits a larger reduction in impedance magnitude after doping, indicating less resistive grain boundaries. A similar reduction in impedance with doping occurs in the IG size samples (Fig. S5 in Supplementary Material). We propose that the larger reduction seen in the IG and CG samples is related to the observed layered structure that forms at the grain boundaries. Bulk P2 structured Na_xCoO_2 possesses attractive Na^+ and e^- transport properties, and forms at the processing temperatures associated with these specific Na-HEO samples [30–32,34].

Phase angle values, as measured for our various Na-HEO samples, exhibit distinct frequency dependencies due to various relaxation mechanisms throughout the microstructure and measurement set up. Phase angle is calculated from the arctangent of the imaginary and real impedance [38,57]. Effectively, phase angle quantifies the lead or lag between an applied voltage and its current response. A phase angle value closer to −90 degrees indicates purely capacitive behavior, while a value of 0 degrees indicates a pure resistor. It can be seen in Fig. 6 A and 6B that the phase angle for FG and CG samples is close to −80 degrees for both doped and undoped samples in the low frequency regime, indicating capacitive behavior. A high phase angle at low frequencies often indicates a more capacitive behavior due to the double layer effect occurring between the blocking electrode and sample [58,61].

In the intermediate frequency regime both doped and undoped FG samples (Fig. 6 A) exhibit phase angle transitions from capacitive to resistive behavior as frequency increases. The transition is related to the relaxation of ions at heterogeneous grain and grain boundary interfaces [58]. The frequency that the transition occurs at can provide insight into the electrical mechanisms. Here we have quantified the transition between capacitive and resistive behavior in the phase angle Bode plots by observing the frequency where the phase angle is equivalent to ~45° [58,59]. Higher frequency phase angle transitions indicate a reduction in charge transfer and relaxation time for the grain and grain boundary interface [57,58,62]. Doping the FG samples with Na causes the phase angle transition to shift toward higher frequencies, indicating reduced charge transfer time [57,58]. In the doped FG samples, we observe the phase angle in the intermediate frequency regime tends to be ~80°, indicating the retention of a capacitive like behavior at higher frequencies compared to the undoped samples (Fig. S5 in Supplementary Material). We attribute this capacitive behavior to Na buildup near the space charge layer where a double layer capacitive effect may be the cause for the high phase angle [58].

For sample CG-Na-HEO, Fig. 6B shows the phase angle transition to resistive behavior within the low frequency regime. Conversely, sample CG-33Na-HEO has a phase angle transition that shifts toward a higher frequency for the grain and grain boundary relaxation mechanism. The shift to higher frequencies is consistent with doping in lithium lanthanum zirconium oxide (LLZO) materials where there is a reduction in the charge transfer and relaxation time at the boundary [58]. Overall, the phase transition associated with reduction in charge transfer and relaxation time at the grain and grain boundary interface shifts to higher frequencies for doped CG samples more so than for doped FG samples. We attribute this shift to higher frequencies to the presence of the observed Na_xCoO_2 layered structure in the doped CG samples, highlighting the importance of this layered structure to the charge transport

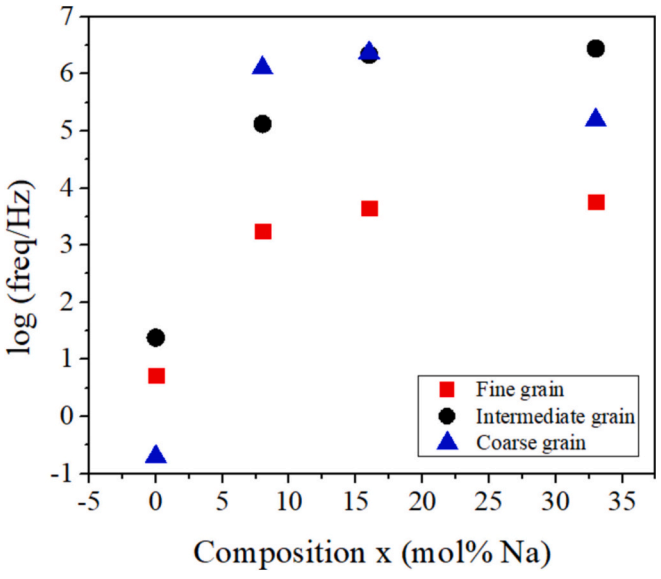

Fig. 7. Relaxation frequencies for bulk HEO and Na-HEO samples.

at the grain boundaries. Fig. 7 displays the phase transition frequency response for all samples. The doped FG samples (shown in red) show a shift at higher frequencies, likely due to the increase in mobile charge carrier ions. The IG and CG samples processed above the P2 Na_xCoO_2 formation temperature (750 °C) have faster relaxation times for the grain boundaries, evident from the higher frequencies observed for the capacitive to resistive transition. For all of our Na-HEO samples, Na doping creates a significant decrease in overall impedance and a reduction in charge transfer and relaxation time for the grain and grain boundary interface. Yet, the presence of the layered structure at the boundaries for IG and CG samples likely contributes significantly more to the reduced charge transfer time.

4.4. Na-HEO activation energy

Ionic transport is strongly dictated by the energy landscape throughout the material. The highest energy barrier(s) along the diffusion path determines the activation energy requirement for an ion to move. It can be expected that an increased number of mobile carriers, changing oxidation states, and oxygen vacancies will affect this barrier. Activation energy measurements obtained from temperature-dependent EIS experiments show that Na doping has a significant influence on the energy barrier for charge transport (Fig. 8). We note that the ensuing section does not discuss the influence of space charge effects on the role of Na doping on the electrical behavior. To consider space charge effects on conductivity it is necessary to know what defects predominantly form in the grain boundaries. The predominant defects which form in the grain boundaries of TM-HEO are not currently known, so it is not obvious if the grain boundaries facilitate local enrichment of oxygen or Na vacancies. We acknowledge that there is insufficient evidence to rule out any space charge effects in our samples. However, our experimental observations show that: (1) $NaCoO_2$ forms between grains, and (2) the oxidation of Co (Fig. 2) seems to be the dominant charge compensation mechanism for strain relief and charge neutrality when Na is added to the structure. From a defect chemistry perspective, we interpret these observations as co-segregation of Na on a transition metal site, Na'_M, and oxidized Co, $Co^{\bullet}_{Co}$, to the grain boundaries, where they form $NaCoO_2$. The presence of the $NaCoO_2$ phase and the oxidation of Co lead to the conclusion that the increase in conductivity with increasing Na doping arises from the presence of the $NaCoO_2$.

The fine grain sample doped with 8 mol% Na (FG-8Na-HEO) exhibits an increase in total activation energy value (E_a) when compared to the undoped sample FG-HEO), 0.26 eV versus 0.14 eV, respectively (Fig. 8 A). These values are consistent with those reported by Bérardan et al. for Na-doped TM-HEO [14]. The E_a values we measured decrease with additional Na doping down to 0.19 eV for sample FG-16Na-HEO and 0.16 eV for sample FG-33Na-HEO. Similar behavior has been shown for other oxide materials, such as Ta-doped Li_2TiO_3.

Using the equivalent circuit method, activation energy values for grain bulk (E_b) and grain boundaries (E_{gb}) were also calculated, as shown in Fig. 8. Overall, the E_b values for the FG samples exhibit a similar trend as the total E_a values for all dopant concentrations, with the highest E_b value of 0.42 eV for sample FG-8Na-HEO. E_{gb} values also exhibit an increase with small doping concentrations but then decrease with increasing dopant concentration above 16 mol%. The E_{gb} values consistently exhibit the lowest activation energy for all doped FG samples, indicating effective ion migration at the boundaries. Multiple perovskites and alumina materials exhibit enhanced ionic transport near or along grain boundaries [63–65]. McGovern et al. hypothesized that ions can become trapped at the boundary initially but allowed to drift normal to the grain boundary channel direction [64]. Conversely, Phung et al. states that activation energies for ion migration in the boundary is lower due to the prevalence of ionic vacancies when compared to the lattice [63]. Observations of high effective grain boundary conductivity and low grain boundary activation energy are reasonable in light of the above previous literature on other electrically conductive ceramics [63–65]. Notably, thus far we find no evidence of the Na_xCoO_2 layered structure in the fine grain samples processed without heat treatments, despite the low values for E_a.

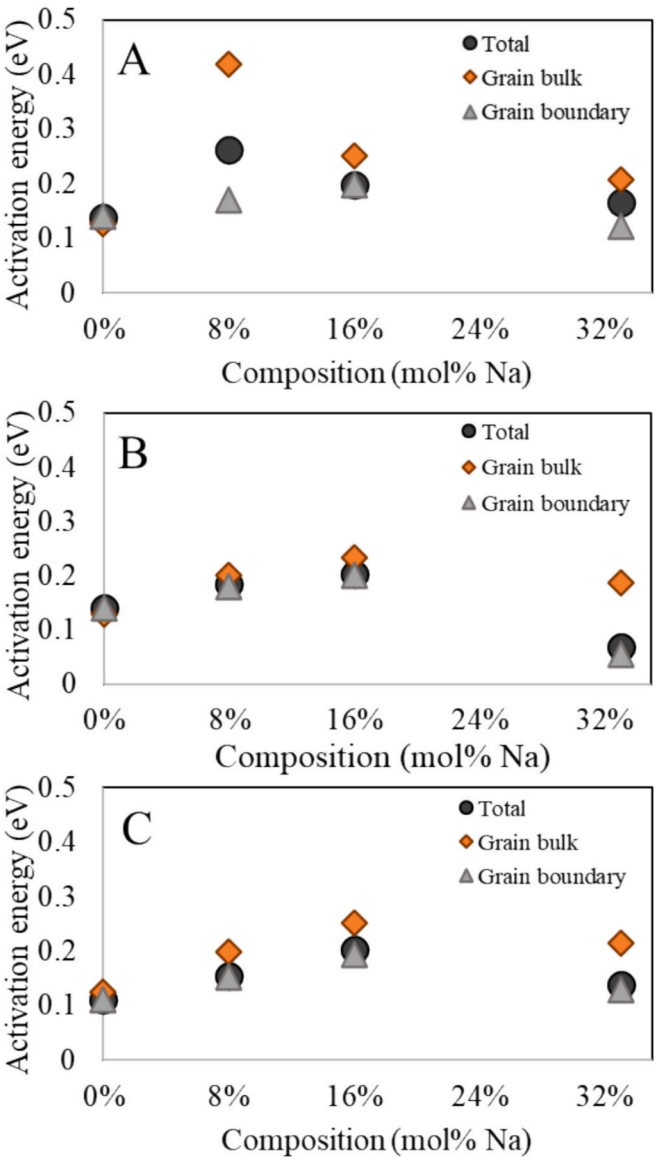

Fig. 8. Activation energy values in eV for: (A) fine, (B) intermediate, and (C) coarse grain samples. Total, grain bulk, and effective grain boundary activation energy are represented as black circles, orange diamonds, and gray triangles, respectively.

IG samples, shown in Fig. 8B, which do contain the boundary structure (Fig. 3), exhibit an increase in both E_b and E_{gb} values with increased dopant concentration up to 16 mol%. The value of E_a for the undoped sample, IG-HEO, is low at 0.14 eV and increases to 0.20 eV when doped with 16 mol% Na. For higher dopant concentrations, the E_a value decreases to 0.06 eV. Overall, the IG samples exhibit lower E_a values when compared to the FG samples. Similar behavior between E_a and dopant concentrations are observed in the CG samples (Fig. 8C).

Values for E_{gb} are consistently lower than the E_b values across all doped samples. We attribute these lower values and the corresponding efficiency of the grain boundary transport to the presence of the P2 Na_xCoO_2 structured phase. For comparison, Table 3 contains both measured [66] and calculated [67] E_a values for various compositions of Na_xCoO_2 and other Na-ion conducting materials. It is important to note

Table 3
| Activation energy values for Na-ion conducting materials and other materials of interest.

Material	Transport mechanism	Activation energy (eV)	References
Na_xCoO_2	Na^+ diffusion/ intercalation	0.2–0.3	[35,67]
Na-HEO, $Na_3In_{1-x}Sc_xCl_6$	Na^+ transport in rocksalt	0.1–0.4	[14,68,69]
TM-HEO single-phase	Cu^+ polaron hopping	0.6–0.8	[22]
TM-HEO multi-phase	$V_{Cu}^{//}/Cu^+/Cu^{2+}$ polaron hopping	0.3–0.5	[22]
Co_3O_4	Co^{2+}/Co^{3+} polaron hopping	0.1–0.4	[73–75]
Li doped NiO	Ni^{2+}/Ni^{3+} polaron hopping	0.1–0.6	[72]
Li-HEO/Na-HEO	Mixed ionic/electronic	0.1–0.2	[27]

that Na_xCoO_2 compositions with lower Na content possess lower values of E_a [67], which is due to the low vacancy concentration at high Na concentrations, strong electrostatic interactions among Na^+ ions, and the Na ordering. As the Na concentration decreases closer to 0.5, the energy barrier is significantly decreased, and the Na^+ acts as a fast ion conductor which can intercalate in the P2 honeycomb sublattice [67]. Compositions of Na_xCoO_2 closer to the fast ion conducting variant (low Na concentration) more closely match with our boundary measurements, and allude to the P2 phase in our samples being deficient in Na. For FG samples there is no obvious evidence of the P2 structure in XRD. However, it is possible that the concentration of the layered phase is below the detection limit of XRD, and thus still contributes to the low value for E_{gb}. Other Na^+ conducting rocksalt type materials, such as α-$NaFeO_2$ and $Na_3In_{1-x}Sc_xCl_6$ [68,69], exhibit E_a values in agreement with our Na-HEO values, in the range of 0.2–0.4 eV (Table 3), indicating that Na^+ within the bulk rocksalt phase could be hopping similarly through the octahedral vacancies via a tetrahedral window (o-t-o) [70,71].

Ranges of activation energy values for electronic transport in transition metal oxides are also shown in Table 3. Vahidi et al. reported on a thermally activated small polaron hopping mechanism of Cu^{1+}/Cu^{2+} pairs for single and multi-phase TM-HEO [22]. Our XPS data does show evidence of a mixed oxidation state for Cu (Fig. S1B in Supplementary Material), but there is very little to no variability in the amount with changes in Na concentration. The E_a measurements from the single and multi-phase TM-HEO study (without Na doping) are also slightly higher than what is reported in the current study for Na-HEO. NiO, when doped with Li, induces an oxidation of Ni to maintain charge neutrality, which increases the transport of holes via Ni^{2+}/Ni^{3+} pairs [72]. The E_a value for Li-doped NiO decreases with increasing Li content, from 0.6 to 0.1 eV. Our results and those by others who have reported on Li-doped HEO exhibit similar decreases in activation energy with increasing alkali metal content [16]. Notably, we do not see any oxidation of Ni^{3+} in our XPS results (Fig. S1C), so the oxidation of Co is likely the carrier for holes. The p-type semiconducting nature of Co_3O_4 spinel is due to polaronic hopping of holes in the form of Co^{2+}/Co^{3+} pairs [73]. The increased oxidation of Co likely enhances a similar hole transport mechanism in our Na-HEO samples, and E_a values for Co_3O_4 fall within the range of measurements listed here (Table 3) [73–75].

The closeness in E_a values for various transport mechanisms can make it difficult to identify a major charge carrier without non-blocking electrodes. However, it is known that Na solubility in silver is very limited [76], so the rate limiting Warburg impedance phenomenon seen in our doped samples would suggest limited Na^+ movement at the electrode interface. Based on this E_a comparison, it is plausible that Na-HEO is a mixed conductor of Na^+ and Co^{2+}/Co^{3+} polaronic type hopping. While previous work has indicated that Na-doped TM-HEO forms oxygen vacancies, we hypothesize that Na is the primary charge carrier during ionic conduction. This hypothesis is partly based on our observations of the Warburg phenomenon during our EIS measurements due to our use of the Na blocking Ag electrodes. Additionally, our activation energy values are similar to those found in other materials that exhibit Na ion transport.

4.5. Na-HEO grain boundary engineering

Our TEM and impedance analysis demonstrate the presence of a layered structure at the grain boundaries of Na-doped TM-HEOs that significantly influences the electrical behavior. Na-containing high entropy layered materials have shown a correlation between entropy stabilization and improved cycle stability [53]. However, none have reported on the possibility of forming a P2 layered structure at the boundaries. We observe that this layer-structured phase appears frequently and has an influence on the boundary conductivity for samples processed above 700 °C or for extended heat treatment times.

A schematic illustrating the interplay between processing temperature, microstructure, and electrical behavior in equimolar Na-HEO (16 mol% Na) is presented in Fig. 9. FG samples exhibit the lowest conductivity. At this grain size, processing temperature, and time the secondary phases are highlighted by a yellow arrow in the adjacent XRD pattern. From EDS and crystallographic databases, it is believed that these are carbonate, oxide, and possibly hydroxide compounds that form at the grain boundaries. Along with no Na_xCoO_2 peaks present in the XRD patterns, FG samples were also processed below the probable Na_xCoO_2 formation temperature of 750 °C, increasing the likelihood of little-to-no layered structure forming at the boundaries. As the consolidation temperature reaches 900 °C, the grain size and conductivity also rise. Sample IG-16Na-HEO reaches 6.61×10^{-6} S•cm^{-1} and the XRD spectra shows no secondary phase peaks around the main (111) rocksalt peaks. However, the samples are processed above the likely Na_xCoO_2 formation temperature and TEM confirms the presence of the layered structure at the boundaries. We hypothesize that the amount of the Na_xCoO_2 phase is below the detectable limits of our XRD instrument. Nevertheless, we believe that the amount of layered structure present directly influences the rise in total conductivity and boundary conductivity, as seen in Figs. 4C and 5. The increase in consolidation temperature to 1000 °C for CG samples has allowed for a high enough temperature to form a higher amount of the Na_xCoO_2 phase. Therefore, the main Na_xCoO_2 peak is visible in the XRD spectra, highlighted by a blue arrow (Fig. 9). The high total (2.42×10^{-5} S•cm^{-1}) and effective grain boundary (5.31×10^{-5} S•cm^{-1}) conductivity are consistent with the presence of Na_xCoO_2 at the grain boundaries.

5. Conclusions

We demonstrate the ability to engineer the grain boundaries of Na-doped high entropy oxide $(Co,Cu,Mg,Ni,Zn)_{1-x}Na_xO$ using composition and processing conditions to leverage the formation of a layer-structured secondary phase. Consolidation temperatures above 700 °C and Na dopant concentrations of 16 mol% or greater directly influence the formation of the Na_xCoO_2 layered structure at the grain boundaries, leading to enhanced conductivity up to 2.4×10^{-5} S•cm^{-1}. Our investigation indicates that this grain boundary structure, as well as a Co charge compensation mechanism occurring in the bulk, contribute to the enhanced conductivity. Activation energy measurements reveal Na-HEO is likely a mixed conductor of Na^+ and Co^{2+}/Co^{3+} polaronic type hopping. Overall, the observation of tunable grain boundary conductivity is an especially important finding to the electroceramics community, where grain boundaries are normally considered inhibitive to electrical conductivity. With these findings, one can engineer the grain boundary conductivity of Na-HEO and take advantage of a new design strategy for Na-ion battery materials.

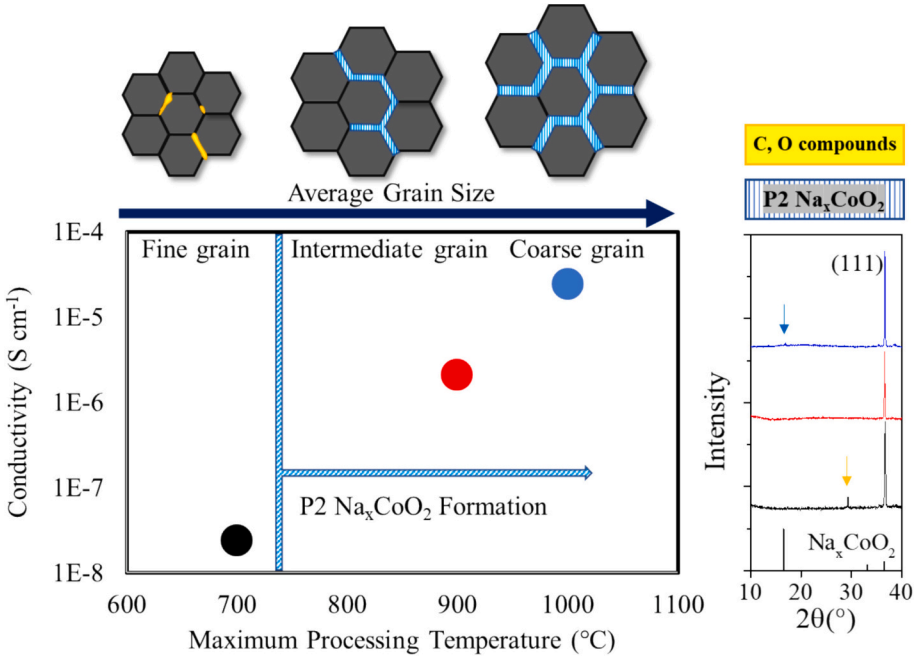

Fig. 9. Schematic of equimolar Na-HEO conductivity vs maximum consolidation temperature, with a blue striped bar at 750 °C representing the formation temperature for Na_xCoO_2. Representation of grain size and additional phases are shown above for the fine (left), intermediate (middle) and coarse (right) grain samples. XRD spectra for Na_xCoO_2, along with fine (black), intermediate (red), and coarse (black) grain samples are provided on the right. Carbon and oxygen compounds are highlighted in the XRD spectra with a yellow arrow, while the layered P2 structure is denoted with a blue arrow.

CRediT authorship contribution statement

Justin Cortez: Writing – original draft, Validation, Investigation, Formal analysis, Conceptualization. **Alexander Dupuy:** Writing – review & editing, Supervision, Conceptualization. **Hasti Vahidi:** Writing – review & editing, Investigation, Formal analysis, Conceptualization. **Yiheng Xiao:** Writing – review & editing, Investigation. **William J. Bowman:** Writing – review & editing, Supervision, Investigation, Funding acquisition, Conceptualization. **Julie M. Schoenung:** Writing – review & editing, Supervision, Resources, Investigation, Funding acquisition, Conceptualization.

Declaration of competing interest

The authors declare that they have no known competing financial interests or personal relationships that could have appeared to influence the work reported in this paper.

Acknowledgements

This research was primarily supported by the National Science Foundation (NSF) Materials Research Science and Engineering Center (MRSEC) through the UC Irvine Center for Complex and Active Materials (DMR-2011967). We also acknowledge the use and access to equipment and facilities at the UC Irvine Materials Research Institute (IMRI) – (including funding from NSF DMR – 2011967).

Appendix A. Supplementary data

Supplementary data to this article can be found online at https://doi.org/10.1016/j.ssi.2024.116745.

Data availability

Data will be made available on request.

References

[1] M. Li, J. Lu, Z. Chen, K. Amine, 30 years of Lithium-ion batteries, Adv. Mater. 30 (2018), https://doi.org/10.1002/adma.201800561.
[2] B. Scrosati, J. Hassoun, Y.K. Sun, Lithium-ion batteries. A look into the future, Energy Environ Sci 4 (2011) 3287–3295, https://doi.org/10.1039/c1ee01388b.
[3] L. Lu, X. Han, J. Li, J. Hua, M. Ouyang, A review on the key issues for lithium-ion battery management in electric vehicles, J. Power Sources 226 (2013) 272–288, https://doi.org/10.1016/j.jpowsour.2012.10.060.
[4] J.W. Fergus, Ion transport in sodium ion conducting solid electrolytes, Solid State Ion. 227 (2012) 102–112, https://doi.org/10.1016/j.ssi.2012.09.019.
[5] E. De La Llave, V. Borgel, K.J. Park, J.Y. Hwang, Y.K. Sun, P. Hartmann, F. F. Chesneau, D. Aurbach, Comparison between Na-ion and Li-ion cells: understanding the critical role of the cathodes stability and the anodes pretreatment on the cells behavior, ACS Appl. Mater. Interfaces 8 (2016) 1867–1875, https://doi.org/10.1021/acsami.5b09835.
[6] J.Y. Hwang, S.T. Myung, Y.K. Sun, Sodium-ion batteries: present and future, Chem. Soc. Rev. 46 (2017) 3529–3614, https://doi.org/10.1039/c6cs00776g.
[7] C. Li, Z. Wang, Z. He, Y. Li, J. Mao, K. Dai, C. Yan, J. Zheng, An advance review of solid-state battery: challenges, progress and prospects, Sustain. Mater. Technol. 29 (2021) e00297, https://doi.org/10.1016/j.susmat.2021.e00297.
[8] J. Janek, W.G. Zeier, Challenges in speeding up solid-state battery development, Nat. Energy 8 (2023) 230–240, https://doi.org/10.1038/s41560-023-01208-9.
[9] C. Shi, L. Wang, X. Chen, J. Li, S. Wang, J. Wang, H. Jin, Challenges of layer-structured cathodes for sodium-ion batteries, Nanoscale Horiz 7 (2021) 338–351, https://doi.org/10.1039/d1nh00585e.
[10] A. Sarkar, L. Velasco, D. Wang, Q. Wang, G. Talasila, L. de Biasi, C. Kübel, T. Brezesinski, S.S. Bhattacharya, H. Hahn, B. Breitung, High entropy oxides for reversible energy storage, Nat. Commun. 9 (2018), https://doi.org/10.1038/s41467-018-05774-5.
[11] N. Qiu, H. Chen, Z. Yang, S. Sun, Y. Wang, Y. Cui, A high entropy oxide ($Mg_{0.2}Co_{0.2}Ni_{0.2}Cu_{0.2}Zn_{0.2}O$) with superior lithium storage performance, J. Alloys Compd. 777 (2019) 767–774, https://doi.org/10.1016/j.jallcom.2018.11.049.
[12] Q. Wang, A. Sarkar, Z. Li, Y. Lu, L. Velasco, S.S. Bhattacharya, T. Brezesinski, H. Hahn, B. Breitung, High entropy oxides as anode material for Li-ion battery applications: a practical approach, Electrochem. Commun. 100 (2019) 121–125, https://doi.org/10.1016/j.elecom.2019.02.001.
[13] N.J. Usharani, R. Shringi, H. Sanghavi, S. Subramanian, S.S. Bhattacharya, Role of size, alio−/multi-valency and non-stoichiometry in the synthesis of phase-pure high entropy oxide (Co,Cu,Mg,Na,Ni,Zn)O, Dalton Trans. 49 (2020) 7123–7132, https://doi.org/10.1039/d0dt00958j.
[14] D. Bérardan, S. Franger, A.K. Meena, N. Dragoe, Room temperature lithium superionic conductivity in high entropy oxides, J. Mater. Chem. A 4 (2016) 9536–9541, https://doi.org/10.1039/C6TA03249D.
[15] M. Moździerz, J. Dąbrowa, A. Stępień, M. Zajusz, M. Stygar, W. Zając, M. Danielewski, K. Świerczek, Mixed ionic-electronic transport in the high-entropy

(Co,Cu,Mg,Ni,Zn)$_{1-x}$Li$_x$O oxides, Acta Mater. 208 (2021) 116735, https://doi.org/10.1016/j.actamat.2021.116735.
[16] N. Osenciat, D. Bérardan, D. Dragoe, B. Léridon, S. Holé, A.K. Meena, S. Franger, N. Dragoe, Charge compensation mechanisms in Li-substituted high-entropy oxides and influence on Li superionic conductivity, J. Am. Ceram. Soc. 102 (2019) 6156–6162, https://doi.org/10.1111/jace.16511.
[17] Z. Rak, C.M. Rost, M. Lim, P. Sarker, C. Toher, S. Curtarolo, J.P. Maria, D. W. Brenner, Charge compensation and electrostatic transferability in three entropy-stabilized oxides: results from density functional theory calculations, J. Appl. Phys. 120 (2016), https://doi.org/10.1063/1.4962135.
[18] J.F. Wu, X. Guo, Origin of the low grain boundary conductivity in lithium ion conducting perovskites: Li$_{3x}$La$_{0.67-x}$TiO$_3$, Phys. Chem. Chem. Phys. 19 (2017) 5880–5887, https://doi.org/10.1039/c6cp07757a.
[19] J. Fleig, J. Maier, The impedance of ceramics with highly resistive grain boundaries: validity and limits of the brick layer model, J. Eur. Ceram. Soc. 19 (1999) 693–696.
[20] T. Van Dijk, A.J. Burggraaf, Grain boundary effects on ionic conductivity in ceramic Gd$_x$Zr$_{1-x}$O$_{2-(x/2)}$ solid solutions, Phys. Status Solidi (a) 63 (1981), https://doi.org/10.1002/pssa.2210630131.
[21] M.J. Verkerk, B.J. Middelhuis, A.J. Burggraaf, Effect of grain boundaries on the conductivity of high-purity ZrO$_2$Y$_2$O$_3$ ceramics, Solid State Ion. 6 (1982) 159–170, https://doi.org/10.1016/0167-2738(82)90083-2.
[22] H. Vahidi, A.D. Dupuy, B.X. Lam, J. Cortez, P. Garg, T.J. Rupert, J.M. Schoenung, W.J. Bowman, Reversible enhancement of electronic conduction caused by phase transformation and interfacial segregation in an entropy-stabilized oxide, Adv. Funct. Mater. 34 (2024) 2315895, https://doi.org/10.1002/adfm.202315895.
[23] L. Lutterotti, M. Bortolotti, G. Ischia, I. Lonardelli, H.R. Wenk, Rietveld texture analysis from diffraction images, Zeitschrift Fur Kristallographie, Supplement 1 (2007) 125–130, https://doi.org/10.1524/zksu.2007.2007.suppl_26.125.
[24] M. Moździerz, J. Dąbrowa, A. Stępień, M. Zajusz, M. Stygar, W. Zając, M. Danielewski, K. Świerczek, Mixed ionic-electronic transport in the high-entropy (Co,Cu,Mg,Ni,Zn)1-xLixO oxides, Acta Mater. 208 (2021), https://doi.org/10.1016/j.actamat.2021.116735.
[25] A.D. Dupuy, X. Wang, J.M. Schoenung, Entropic phase transformation in nanocrystalline high entropy oxides, Mater Res Lett 7 (2019) 60–67, https://doi.org/10.1080/21663831.2018.1554605.
[26] E.L.S. dos Veiga, M. Fortuno-Morte, H. Beltran-Mir, E. Cordoncillo, Effect of the oxidation states on the electrical properties of Fe-doped Pr$_2$Zr$_2$O$_7$ pyrochlore, J. Mater. Res. Technol. 16 (2022) 201–215, https://doi.org/10.1016/j.jmrt.2021.11.146.
[27] A. Natoli, B.I. Arias-Serrano, E. Rodríguez-Castellón, A. Żurawska, J.R. Frade, A. A. Yaremchenko, Mixed ionic-electronic conductivity, redox behavior and thermochemical expansion of mn-substituted 5YSZ as an interlayer material for reversible solid oxide cells, Materials 14 (2021) 1–23, https://doi.org/10.3390/ma14030641.
[28] T.J. Chuang, C.R. Brundle, D.W. Rice, Interpretation of the x-ray photoemission spectra of cobalt oxides and cobalt oxide surfaces, Surf. Sci. 59 (1976) 413–429, https://doi.org/10.1016/0039-6028(76)90026-1.
[29] D. Gallant, M. Pézolet, S. Simard, Optical and physical properties of cobalt oxide films electrogenerated in bicarbonate aqueous media, J. Phys. Chem. B 110 (2006) 6871–6880, https://doi.org/10.1021/jp056689h.
[30] I. Terasaki, Y. Sasago, K. Uchinokura, Large thermoelectric power in single crystals, Phys. Rev. B Condens Matter Mater. Phys. 56 (1997) R12685–R12687, https://doi.org/10.1103/PhysRevB.56.R12685.
[31] B. Raveau, Transition metal oxides: promising functional materials, J. Eur. Ceram. Soc. 25 (2005) 1965–1969, https://doi.org/10.1016/j.jeurceramsoc.2005.03.220.
[32] C. Delmas, J.J. Braconnier, C. Fouassier, P. Hagenmuller, Electrochemical intercalation of sodium in Na$_x$CoO$_2$ bronzes, Solid State Ion. 3–4 (1981) 165–169, https://doi.org/10.1016/0167-2738(81)90076-X.
[33] A.D. Dupuy, J.M. Schoenung, Morphological evolution in nanostructured secondary phases in entropy stabilized oxides, Mater Charact 193 (2022) 112301, https://doi.org/10.1016/j.matchar.2022.112301.
[34] Y. Lei, X. Li, L. Liu, G. Ceder, Synthesis and stoichiometry of different layered sodium cobalt oxides, Chem. Mater. 26 (2014) 5288–5296, https://doi.org/10.1021/cm5021788.
[35] S. Guo, Y. Sun, J. Yi, K. Zhu, P. Liu, Y. Zhu, G.Z. Zhu, M. Chen, M. Ishida, H. Zhou, Understanding sodium-ion diffusion in layered P2 and P3 oxides via experiments and first-principles calculations: a bridge between crystal structure and electrochemical performance, NPG Asia Mater. 8 (2016) 266, https://doi.org/10.1038/am.2016.53.
[36] P. Mandal, Anomalous transport properties of co-site impurity doped NaxCoO$_2$, J. Appl. Phys. 104 (2008), https://doi.org/10.1063/1.2978212.
[37] I. Terasaki, I. Tsukada, Y. Iguchi, Impurity-induced transition and impurity-enhanced thermopower in the thermoelectric oxide NaCo$_{2-x}$Cu$_x$O$_4$, Phys. Rev B 65 (2002) 195106, https://doi.org/10.1103/PhysRevB.65.195106.
[38] P. Vadhva, J. Hu, M.J. Johnson, R. Stocker, M. Braglia, D.J.L. Brett, A.J.E. Rettie, Electrochemical impedance spectroscopy for all-solid-state batteries: theory, methods and future outlook, ChemElectroChem 8 (2021) 1930–1947, https://doi.org/10.1002/celc.202100108.
[39] J.T.S. Irvine, D.C. Sinclair, A.R. West, Electroceramics: characterization by impedance spectroscopy, Adv. Mater. 2 (1990) 132–138, https://doi.org/10.1002/ADMA.19900020304.
[40] G. Gregori, R. Merkle, J. Maier, Ion conduction and redistribution at grain boundaries in oxide systems, Prog. Mater. Sci. 89 (2017) 252–305, https://doi.org/10.1016/j.pmatsci.2017.04.009.
[41] E. Casero, A.M. Parra-Alfambra, M.D. Petit-Domínguez, F. Pariente, E. Lorenzo, C. Alonso, Differentiation between graphene oxide and reduced graphene by electrochemical impedance spectroscopy (EIS), Electrochem. Commun. 20 (2012) 63–66, https://doi.org/10.1016/j.elecom.2012.04.002.
[42] H. Ding, T. Wu, S. Zhao, H. Sun, J. Li, X. Guo, P. Wang, Grain boundary conduction behaviors of ultra-fine grained CeO$_2$/BaCeO$_3$ based electrolytes, Ceram. Int. 48 (2022) 25314–25321, https://doi.org/10.1016/j.ceramint.2022.05.204.
[43] H.C. Graham, N.M. Tallan, R. Russell, Particle size dependence of the electrical conductivity of NaCl, J. Am. Ceram. Soc. 50 (1967) 156–163, https://doi.org/10.1111/j.1151-2916.1967.tb15068.x.
[44] C. Peters, A. Weber, B. Butz, D. Gerthsen, E. Ivers-Tiffée, Grain-size effects in YSZ thin-film electrolytes, J. Am. Ceram. Soc. 92 (2009) 2017–2024, https://doi.org/10.1111/j.1551-2916.2009.03157.x.
[45] D. Stroud, Generalized effective-medium approach to the conductivity of an inhomogeneous material, Phys. Rev. B 12 (1975) 3368–3373, https://doi.org/10.1103/PhysRevB.12.3368.
[46] A.R. Denton, N.W. Ashcroft, Vegard's law, Phys Rev A (Coll Park) 43 (1991).
[47] J.G. Kim, D.L. Pugmire, D. Battaglia, M.A. Langell, Analysis of the NiCo$_2$O$_4$ spinel surface with auger and X-ray photoelectron spectroscopy, Appl. Surf. Sci. 165 (2000) 70–84, https://doi.org/10.1016/S0169-4332(00)00378-0.
[48] A.D. Dupuy, I.-T. Chiu, P. Shafer, E. Arenholz, Y. Takamura, J.M. Schoenung, Hidden transformations in entropy-stabilized oxides, J. Eur. Ceram. Soc. (2021), https://doi.org/10.1016/j.jeurceramsoc.2021.06.014.
[49] M. Song, X. Zhang, S. Wan, G. Wang, J. Liu, W. Li, H. Dong, C. Lou, Z. Chen, B. Chen, H. Zhang, Electrical conductivities and conduction mechanism of Lithium-doped high-entropy oxides at different temperature and pressure conditions, JACS Au 4 (2024) 592–606, https://doi.org/10.1021/jacsau.3c00693.
[50] Y. Inaguma, J. Yu, Y. Shan, M. Itoh, T. Nakamuraa, The effect of the hydrostatic pressure on the ionic conductivity in a perovskite lanthanum Lithium Titanate, J. Electrochem. Soc. 142 (1995) L8–L11, https://doi.org/10.1149/1.2043988.
[51] V. Faka, M.T. Agne, P. Till, T. Bernges, M. Sadowski, A. Gautam, K. Albe, W. G. Zeier, Pressure dependence of ionic conductivity in site disordered lithium superionic argyrodite Li$_6$PS$_5$Br, energy, Advances 2 (2023) 1915–1925, https://doi.org/10.1039/D3YA00424D.
[52] E. Lökçü, Ç. Toparli, M. Anik, Electrochemical Performance of (MgCoNiZn) $_{1-x}$ Li $_x$ O High-Entropy Oxides in Lithium-Ion Batteries, ACS Appl. Mater. Interfaces 12 (2020) 23860–23866, https://doi.org/10.1021/acsami.0c03562.
[53] S. Yan, S. Luo, L. Yang, J. Feng, P. Li, Q. Wang, Y. Zhang, X. Liu, Novel P2-type layered medium-entropy ceramics oxide as cathode material for sodium-ion batteries, J. Adv. Ceram. 11 (2022) 158–171, https://doi.org/10.1007/s40145-021-0524-8.
[54] F. Ding, C. Zhao, D. Xiao, X. Rong, H. Wang, Y. Li, Y. Yang, Y. Lu, Y.-S. Hu, Using high-entropy configuration strategy to design Na-ion layered oxide cathodes with superior electrochemical Performanceand thermal stability, J. Am. Chem. Soc. 144 (2022) 36, https://doi.org/10.1021/jacs.2c02353.
[55] C. Zhao, F. Ding, Y. Lu, L. Chen, Y.-S. Hu, High-entropy layered oxide cathodes for sodium-ion batteries, Angew. Chem. 132 (2020) 270–275, https://doi.org/10.1002/ange.201912171.
[56] C. Fouassier, G. Matejka, J.M. Reau, P. Hagenmuller, Sur de nouveaux bronzes oxygénés de formule Na$_\chi$CoO$_2$ (χ1). Le système cobalt-oxygène-sodium, J. Solid State Chem. 6 (1973) 532–537, https://doi.org/10.1016/S0022-4596(73)80011-8.
[57] N. Goswami, M.S. Indu, R. Murugan, R. Kant, Experimental corroboration of theory for impedance response of solid electrolytes: doped cubic garnet LLZO, J. Electroanal. Chem. 897 (2021), https://doi.org/10.1016/j.jelechem.2021.115611.
[58] N. Goswami, R. Kant, Theory for impedance response of grain and grain boundary in solid state electrolyte, J. Electroanal. Chem. 835 (2019) 227–238, https://doi.org/10.1016/j.jelechem.2019.01.035.
[59] R. Wang, K. Sun, Y. Zhang, B. Li, C. Qian, J. Li, F. Liu, W. Bao, Nanoscale interface engineering of inorganic solid-state electrolytes for high-performance alkali metal batteries, J. Colloid Interface Sci. 621 (2022) 41–66, https://doi.org/10.1016/J.JCIS.2022.04.075.
[60] I.M. Hodge, M.D. Ingram, A.R. West, Impedance and modulus spectroscopy of polycrystalline solid electrolytes, J. Electroanal. Chem. 74 (1976) 125–143, https://doi.org/10.1016/S0022-0728(76)80229-X.
[61] K.S. Jyotheender, C. Srivastava, Correlating the five-parameter grain boundary character distribution and corrosion behavior of zinc-carbon nanotube composite coatings, Metall. Mater. Trans. A Phys. Metall. Mater. Sci. 52 (2021) 364–377, https://doi.org/10.1007/s11661-020-06070-y.
[62] W.C. Ribeiro, E. Joanni, R. Savu, P.R. Bueno, Nanoscale effects and polaronic relaxation in CaCu$_3$Ti$_4$O$_{12}$ compounds, Solid State Commun. 151 (2011) 173–176, https://doi.org/10.1016/J.SSC.2010.10.034.
[63] N. Phung, A. Al-Ashouri, S. Meloni, A. Mattoni, S. Albrecht, E.L. Unger, A. Merdasa, A. Abate, The role of grain boundaries on ionic defect migration in metal halide perovskites, Adv. Energy Mater. 10 (2020), https://doi.org/10.1002/aenm.201903735.
[64] L. McGovern, I. Koschany, G. Grimaldi, L.A. Muscarella, B. Ehrler, Grain Size Influences Activation Energy and Migration Pathways in MAPbBr$_3$ Perovskite Solar Cells, J. Phys. Chem. Lett. 12 (2021) 2423–2428, https://doi.org/10.1021/acs.jpclett.1c00205.
[65] Y. Lei, Y. Gong, Z. Duan, G. Wang, Density functional calculation of activation energies for lattice and grain boundary diffusion in alumina, Phys. Rev. B Condens Matter Mater. Phys. 87 (2013) 214105, https://doi.org/10.1103/PhysRevB.87.214105.

[66] T. Shibata, Y. Fukuzumi, W. Kobayashi, Y. Moritomo, Fast discharge process of layered cobalt oxides due to high Na^+ diffusion, Sci. Rep. 5 (2015), https://doi.org/10.1038/srep09006.
[67] Y. Mo, S.P. Ong, G. Ceder, Insights into diffusion mechanisms in P2 layered oxide materials by first-principles calculations, Chem. Mater. 26 (2014) 5208–5214, https://doi.org/10.1021/cm501563f.
[68] M.C. Blesa, E. Moran, C. León, J. Santamaria, J.D. Tornero, N. Menéndez, α-$NaFeO_2$: ionic conductivity and sodium extraction, Solid State Ion. 126 (1999) 81–87, https://doi.org/10.1016/S0167-2738(99)00145-9.
[69] F. Hussain, P. Yu, J. Zhu, H. Xia, Y. Zhao, W. Xia, Theoretical prediction of spinel $Na_2In_xSc_{0.666-x}Cl_4$ and rock-salt $Na_3In_{1-x}Sc_xCl_6$ superionic conductors for all-solid-state sodium-ion batteries, Adv. Theory Simul. 6 (2023) 2200569, https://doi.org/10.1002/adts.202200569.
[70] J. Lee, A. Urban, X. Li, D. Su, G. Hautier, G. Ceder, Unlocking the potential of cation-disordered oxides for rechargeable lithium batteries, Science 343 (2014) (1979) 519–522, https://doi.org/10.1126/science.1246432.
[71] Z. Lun, B. Ouyang, D.H. Kwon, Y. Ha, E.E. Foley, T.Y. Huang, Z. Cai, H. Kim, M. Balasubramanian, Y. Sun, J. Huang, Y. Tian, H. Kim, B.D. McCloskey, W. Yang, R.J. Clément, H. Ji, G. Ceder, Cation-disordered rocksalt-type high-entropy cathodes for Li-ion batteries, Nat. Mater. 20 (2021) 214–221, https://doi.org/10.1038/s41563-020-00816-0.
[72] K.V. Rao, A. Smakula, Dielectric properties of cobalt oxide, nickel oxide, and their mixed crystals, J. Appl. Phys. 36 (1965) 2031–2038, https://doi.org/10.1063/1.1714397.
[73] C.S. Cheng, M. Serizawa, H. Sakata, T. Hirayama, Electrical conductivity of Co_3O_4 films prepared by chemical vapour deposition, Mater. Chem. Phys. 53 (1998) 225–230, https://doi.org/10.1016/S0254-0584(98)00044-3.
[74] R.M. Al-Tuwirqi, A.A. Al-Ghamdi, F. Al-Hazmi, F. Alnowaiser, A.A. Al-Ghamdi, N. A. Aal, F. El-Tantawy, Synthesis and physical properties of mixed Co_3O_4/CoO nanorods by microwave hydrothermal technique, Superlattices Microstruct 50 (2011) 437–448, https://doi.org/10.1016/j.spmi.2011.06.007.
[75] S.A. Makhlouf, Z.H. Bakr, K.I. Aly, M.S. Moustafa, Structural, electrical and optical properties of Co_3O_4 nanoparticles, Superlattice. Microst. 64 (2013) 107–117, https://doi.org/10.1016/j.spmi.2013.09.023.
[76] A.D. Pelton, The ag-Na (silver-sodium) system, Bull. Alloy Phase Diagr. 7 (1986) 133–136, https://doi.org/10.1007/BF02881549.